Journal of Applied Physics ARTICLE pubs.aip.org/aip/jap

Coupling of terahertz radiations to tunneling junction: Quantitative determination of amplitude for weak fields

Cite as: J. Appl. Phys. **140**, 014301 (2026); doi: 10.1063/5.0336854
Submitted: 2 April 2026 · Accepted: 15 June 2026 ·
Published Online: 1 July 2026

View Online Export Citation CrossMark

Hüseyin Azazoglu, Rolf Möller, and Manuel Gruber[a)]

AFFILIATIONS

Faculty of Physics and CENIDE, University of Duisburg–Essen, 47057 Duisburg, Germany

Note: This paper is part of the Special Topic on Terahertz Frontiers: Quantum and Emergent Materials, Nanoscale Phenomena, Devices and Applications.
[a)]**Author to whom correspondence should be addressed:** manuel.gruber@uni-due.de

ABSTRACT

Lightwave-driven terahertz scanning tunneling microscopy has attracted considerable interest due to its ability to combine sub-ångström spatial resolution with sub-picosecond temporal resolution. Such measurements require accurate knowledge of the THz near-field transient generated upon coupling the far-field pulse into the junction. Conventional approaches rely on the onset of strong nonlinearity in current–voltage characteristics measured at constant tip–sample distance. Here, combining simulations with experiments exploiting the conduction-band onset of NaCl bilayers on Ag(111), we analyze the determination of the transient amplitude, with particular emphasis on the small-amplitude regime ($\lesssim$0.5 V). We show that the intrinsic broadening of electronic nonlinearities significantly complicates amplitude extraction. We, therefore, introduce an alternative approach based on constant-current spectroscopy, in which the THz-induced current is measured as a function of sample voltage while the feedback loop maintains a fixed DC current. This method yields a pronounced spectral peak whose amplitude, width, and onset are all sensitive to the transient voltage amplitude, providing multiple independent observables for a more robust determination.

I. INTRODUCTION

Numerous processes at the atomic scale occur on ultrafast timescales, including vibrations, charge transfer, and quasiparticle excitations. Accessing these phenomena with temporal resolution comparable to their intrinsic dynamics, while retaining atomic spatial resolution, is essential for elucidating the underlying physical mechanisms.

The emergence of lightwave-driven terahertz scanning tunneling microscopy (THz-STM) provides a solution to this challenge by combining the sub-ångström spatial resolution of STM with the (sub-)picosecond temporal resolution of terahertz spectroscopy,[1] while mitigating thermal effects associated with visible-light excitation.[2–5] In this approach, phase-stable single-cycle THz pulses are coupled to the STM junction, where the metallic tip acts as an antenna that enhances the local electric field.[1,6–8] The enhanced field induces an ultrafast transient voltage across the tip–sample gap which, through the intrinsic nonlinearity of the tunneling current–voltage characteristic, generates a rectified current that is generally detected using lock-in techniques (see, for instance, corresponding descriptions in Refs. 9 and 10).

This methodology has enabled studies of a broad range of ultrafast phenomena, including vibrational dynamics in single pentacene molecules,[11] charge-density-wave dynamics,[12] phase transitions,[13] and lattice vibrations in 2D materials,[14,15] as well as the dynamics of a single H_2 molecule in an STM cavity.[16] Ultrafast THz pulses can also generate forces on sub-picosecond timescales, enabling coherent hindered rotation of a single molecule[17] or the launch of acoustic wave packets.[18] In addition, THz excitation enables STM operation at vanishing DC voltages, thereby reducing perturbation of the system under study. This approach has been used, for example, to probe rapidly decaying orbitals of graphene nanoribbons on Au(111).[19] Further aspects of light–matter interaction at the nanoscale are reviewed in Refs. 20–22. Continuous-wave THz excitation has also been employed to investigate single-molecule vibrational dynamics.[23]

In these experiments, accurate knowledge of the THz waveform at the junction is essential. It has been shown that coupling to the STM junction leads to a low-pass filtering of the incident waveform, thereby modifying its temporal profile.[7] In addition, surface plasmons propagating along the tip and undergoing reflections further reshape the transient voltage at the junction.[24] Current approaches for reconstructing the transient voltage rely on the combination of strong and weak THz pulses.[25–27] In these schemes, a measurable current is generated primarily at the maximum field of the strong pulse. Because the electric fields add linearly, the peak field is modulated by the value of the weak pulse at that instant. By scanning the relative delay between the pulses, the temporal profile of the weak field—and thus of the THz-induced transient voltage—can be reconstructed. This enables time-domain spectroscopy by monitoring modifications of the waveform induced by the system dynamics.[27]

Quantifying the amplitude of the near-field THz voltage is equally important. Early approaches compared current–voltage characteristics acquired in constant-height mode with and without strong THz illumination, combined with simulations of the THz-induced current,[9,28] hereafter referred to as THz current. However, this method requires transient voltages of several volts. A more direct approach exploits strongly nonlinear current–voltage characteristics, such as those associated with molecular orbitals[11] or defects in 2D materials.[29] The voltage at which the nonlinearity occurs is determined from conventional spectroscopy at constant tip–sample distance. Under THz illumination, when the sum of DC and transient voltages reaches this regime, the THz current varies sharply. The transient amplitude can, therefore, be inferred by tracking these sharp changes while sweeping the DC voltage or the THz field amplitude. Extending this approach, Bobzien *et al.* mapped the THz current as a function of both DC voltage and THz amplitude,[29] yielding diamond-like structures. For an onset-type nonlinearity, the slopes of these features directly reflect the extrema of the transient voltage. These methods, however, require spectroscopic features significantly sharper than the transient amplitude. As typical electronic features are several hundred millivolts wide, they are not well suited for determining sub-volt THz amplitudes.

Here, we further analyze the impact of a broad onset of nonlinearity on the determination of the transient voltage amplitude. The commonly used onset-position method exhibits significant limitations in the regime of small amplitudes. We, therefore, introduce an alternative approach in which the THz current is measured as a function of sample voltage under constant-current conditions, rather than at constant height. Supported by simulations, we show that this method provides a strong dynamical response even for sub-volt transient amplitudes, and that multiple observables of the spectra are sensitive to V_{THz}. We experimentally compare both approaches using the conduction-band onset of NaCl bilayer islands on Ag(111). While the two methods yield comparable estimates of the transient amplitude, the constant-current approach offers additional redundancy, thereby reducing uncertainties through the use of multiple independent observables. An additional advantage of this measurement mode is that it allows spectroscopy to be performed while maintaining a low DC over the entire voltage range. This is particularly important at high sample voltages, where constant-height measurements would otherwise lead to large tunneling currents that can destabilize or damage the STM junction.

II. MODELS AND SIMULATIONS

In this section, we consider (i) a prescribed transient voltage waveform at the STM junction (red trace in Fig. 1) and (ii) representative current–voltage (I–V) and tip–sample distance–voltage (z–V) characteristics inspired by measurements on bilayer NaCl on Ag(111). We assume that the electronic properties of the junction are not modified by the transient voltage, i.e., no transient changes of the I–V and z–V characteristics are considered. Under this assumption, we compute the THz current I_{THz} as a function of the DC sample voltage V_{DC} for different amplitudes of the transient voltage V_{THz}, yielding $I_{\mathrm{THz}}(V_{\mathrm{DC}})$ curves for each V_{THz}. Thereafter, $I_{\mathrm{THz}}(V_{\mathrm{DC}})$ is referred to as THz spectrum.

We consider two measurement schemes. The first corresponds to constant tip–sample distance (feedback loop disabled), which is the most intuitive configuration and the one commonly used in reconstruction algorithms.[28,30] We will, in particular, examine the limitations of this approach for small V_{THz}.

The second scheme corresponds to DC voltage sweeps performed under constant current (feedback loop active), where the electronic information of the junction is encoded in $\Delta z(V)$ rather than in $I(V)$, where Δz describe the tip retraction during the voltage sweep (Refs. 31 and 32). We show that, although less intuitive, this approach is better suited for calibrating small V_{THz}.

For conciseness, we refer to THz spectra acquired in constant-height and constant-current modes. In the latter case, the total DC is maintained by the feedback loop, with I_{THz} representing only a small fraction of the total current.

A. Constant-height THz spectra

The considered $I(V)$ characteristics are shown in Fig. 1(a), and their analytical expressions are given in Appendix A. Previous calibration approaches rely on the onset of strong nonlinearity in the tunneling current.[11,29] The black curve represents an idealized case with an abrupt transition from a linear to an exponential regime at a threshold voltage $V_t = 3.0$ V. Since the linear regime does not produce rectification, a transient voltage within this range does not generate any THz current. A finite THz current is only obtained when the sum of V_{DC} and the transient amplitude V_{THz} exceeds V_t. While this model is useful for illustration, the discontinuity in its first derivative at V_t may introduce nonphysical artifacts. We further consider two additional models (red and blue curves), in which the transition is smoothed using a parameter σ, yielding $I(V_{\mathrm{DC}})$ characteristics that are more representative of experimental data.

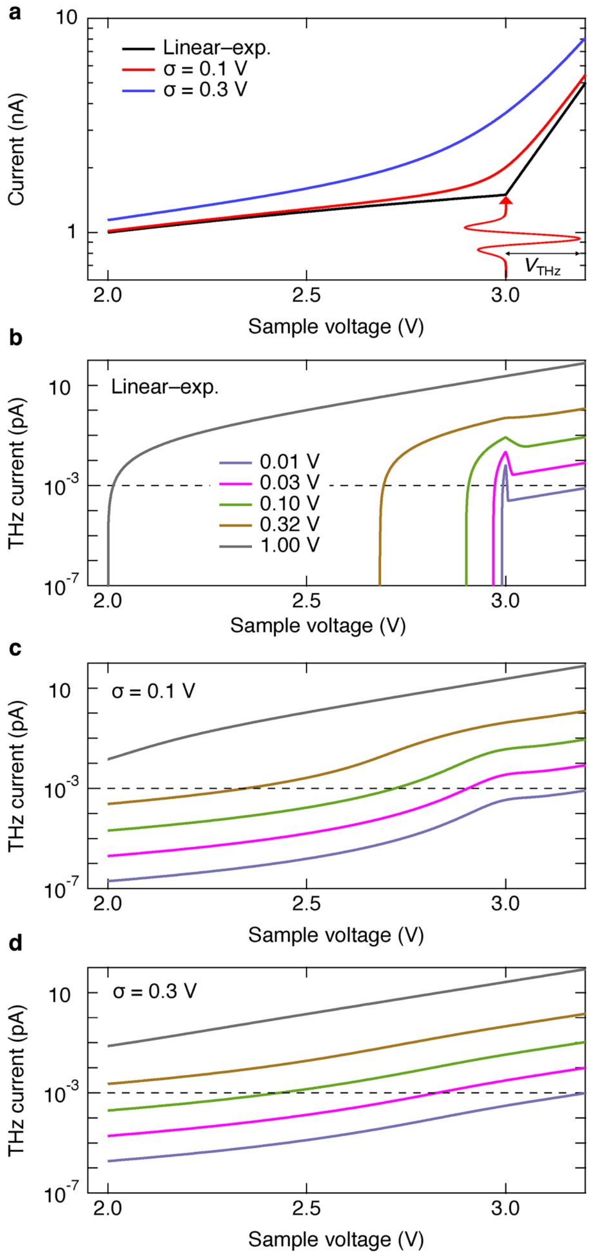

FIG. 1. Simulated rectification of THz voltage transients in constant-height mode. (a) Idealized current–voltage characteristic (black curve) with a sharp transition from linear to exponential behavior at 3.0 V. The characteristics shown in red and blue have additional smoothing (see Appendix A). The red line depicts the temporal evolution of a transient voltage pulse with amplitude V_{THz}, as induced by coupling THz radiation to the STM junction. (b)–(d) Simulated THz spectra for different amplitudes V_{THz} as indicated in the legend using the $I(V)$ characteristic with respectively sharp, smoothed with $\sigma = 0.1$ V and smoothed with $\sigma = 0.3$ V transitions. The horizontal dashed lines indicate a THz current of 1 fA, used here as an optimistic reference level. THz currents of this magnitude are experimentally challenging to measure and fall below the detection limit of many instruments.

The transient voltage waveform $v_{THz}(t)$ is modeled as the difference of two derivatives of Gaussian functions,

$$v_{THz}(t) = \frac{V_{THz}}{N}\left[t\, e^{-\frac{t^2}{2w_1^2}} - A_2\,(t - t_D)\, e^{-\frac{(t-t_D)^2}{2w_2^2}}\right], \qquad (1)$$

where N is a normalization factor chosen such that $v_{THz}(t)$ has a peak amplitude V_{THz}. Using $t_D = 1$ ps, $w_1 = w_2 = 0.77/\sqrt{2}$ ps, and $A_2 = 1/1.4$, the resulting waveform [red trace in Fig. 1(a)] closely resembles the experimentally observed shape,[10] while ensuring numerical stability and reduced noise sensitivity. The time integral of $v_{THz}(t)$ vanishes within numerical precision, consistent with the free-space propagation of the THz electric field from which the transient voltage at the junction is derived. The waveform used throughout the paper is shown as the black curve in Fig. 8(a).

For a given V_{DC}, the transient current is given by

$$i_{THz}(t) = I(V_{DC} + v_{THz}(t)) - I(V_{DC}), \qquad (2)$$

which yields a constant THz current

$$I_{THz} = f_{Rep} \int_0^{1/f_{Rep}} i_{THz}(t)\, dt, \qquad (3)$$

where f_{Rep} is the repetition rate of the THz pulses. I_{THz} is the experimentally accessible quantity.

We first consider the case of a sharp linear–exponential transition. Figure 1(b) shows calculated constant-height THz spectra for different values of V_{THz} (semi-logarithmic scale). For $V_{THz} = 1$ V (grey curve), the onset of the THz current occurs at $V_{DC} = 2.0$ V, corresponding to $V_t - V_{THz}$, as expected. For smaller amplitudes, $V_{THz} = 0.32$ V (brown curve) and $V_{THz} = 0.01$ V (light violet curve), the onset shifts to higher voltages, $V_{DC} \approx 2.68$ V and $V_{DC} \approx 2.99$ V, respectively.

The magnitude of the THz current depends strongly on the tip–sample distance, i.e., on the tunneling parameters. Here, we assume a current of 1 nA at $V_{DC} = 2$ V. In these conditions, a detection threshold on the order of 1 fA (dashed lines in Fig. 1) is required to identify the onsets. This small detection threshold may, in principle, be increased by reducing the tip–sample distance. However, reaching these onset voltages requires large V_{DC}, which combined to large DC tunneling currents may lead to junction instability or damage. This already highlights the difficulty of determining small V_{THz} when V_t is large.

When the transition in $I(V)$ is smoothed [Figs. 1(c) and 1(d), with $\sigma = 0.1$ and 0.3 V, respectively], the onset of the THz current becomes significantly less pronounced. Instead, I_{THz} increases gradually with V_{DC}. For example, for $\sigma = 0.3$ and $V_{THz} = 0.32$ V [brown curve in Fig. 1(d)], the THz current increases from 2×10^{-3} pA at $V_{DC} = 2$ V to ≈1.4 pA at $V_{DC} = 3.2$ V, without a well-defined onset.

At these voltages, the relative magnitude of the THz current is also unfavorable. At $V_{DC} = 3.0$ V, we obtain $I_{THz} \approx 0.46$ pA (for $\sigma = 0.3$ and $V_{THz} = 0.32$ V) for a DC of $I_{DC} \approx 3.6$ nA, corresponding to a ratio of ~10^{-4}. Moreover, a reliable determination of V_{THz} requires *precise* measurements of both the I–V characteristic and the THz spectra. In particular, accurately measuring the I–V characteristic over a wide dynamic range is not straightforward, as further illustrated in Sec. III B.

In summary, determining small transient voltage amplitudes from the nonlinearity of $I(V)$ at large V_{DC} is inherently challenging, especially when the transition to the nonlinear regime is not well defined.

B. Constant-current THz spectra

For constant-current spectroscopic measurements, the feedback loop retracts the tip as the sample voltage is increased in order to maintain a constant current I_{DC}. The electronic information of the junction is, therefore, encoded in $\Delta z(V)$ curves. The interpretation is less direct than in constant-height measurements. However, this approach avoids excessively large currents at high voltages (and very small currents at low voltages), thereby providing a wide dynamic range for spectroscopy. This advantage has been widely exploited to record $dI/dV(V)|_{I=\mathrm{const}}$ spectra. Under suitable assumptions on the tunneling process, and using the measured $\Delta z(V)$, such spectra can be converted into conventional $dI/dV(V)|_{z=\mathrm{const}}$ spectra.[31,32] Our approach follows a similar strategy: based on experimentally constrained assumptions, we reconstruct THz spectra.

As an illustrative example, we use the $\Delta z(V)$ curve shown in Fig. 2(a) (see Appendix B for details). For $V_{DC} \gtrsim 3$ V, the differential conductance increases strongly due to tunneling into the conduction band (e.g., of a NaCl bilayer), which forces a rapid tip retraction to maintain a constant current.

An important aspect of these measurements is the finite response time of the feedback loop. While the feedback is sufficiently fast to follow changes in V_{DC}, it is too slow to respond to the THz-induced voltage transient. As a result, I_{DC} remains effectively constant during the transient, while a rectification process similar to that described in Sec. II A takes place. In practice, the rectification occurs with an effective $I(V)|_{z=\mathrm{const}}$ characteristic, but the tip height z depends on V_{DC} and, therefore, modifies this characteristic.

Rather than measuring $I(V)|_{z=\mathrm{const}}$ explicitly at each tip–sample distance, we reconstruct it from the measured $\Delta z(V)$, assuming small transient amplitudes V_{THz}. For illustration, consider an $I(V)|_{z=\mathrm{const}}$ curve with a sharp increase near a voltage V_1 and a much weaker variation near V_2. In constant-current operation, a small increase of V above V_1 leads to a strong tip retraction, whereas Δz remains nearly constant near V_2. In the following, we derive a relation linking these quantities.

The tunneling current depends on both voltage V and tip–sample distance z and is written as[33]

$$I(V, z) = f(V)\,\exp(-2\kappa z), \quad (4)$$

where κ is the decay constant and $f(V)$ is an unknown function. Under constant-current conditions, $I(V, z) = I_0$ and $z \to \Delta z(V)$,

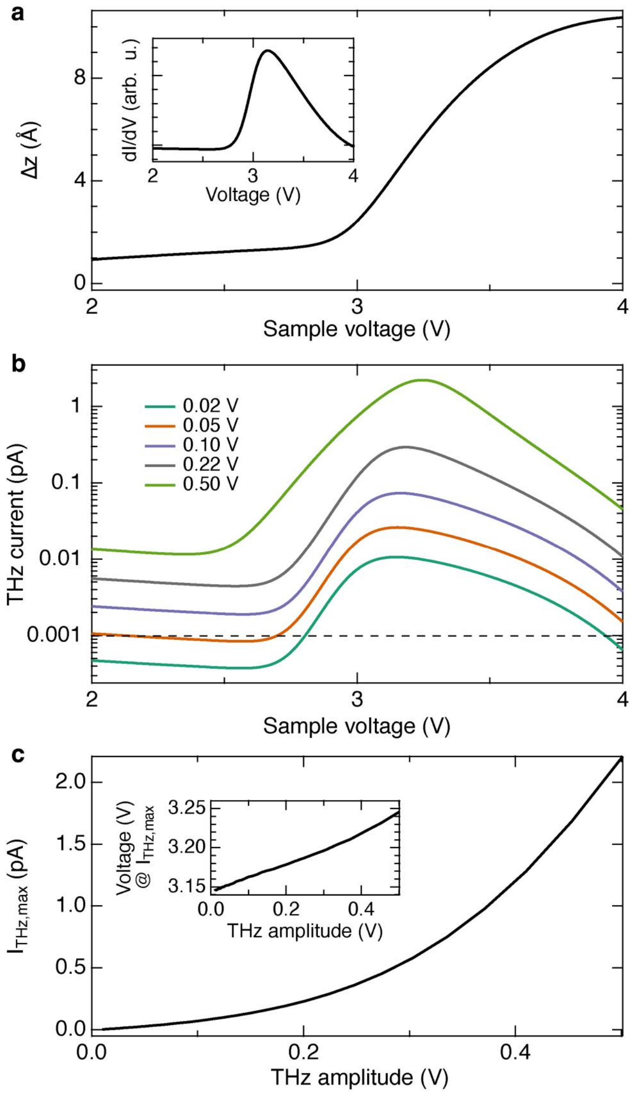

FIG. 2. Simulated rectification of THz voltage pulses in constant-current mode. (a) Assumed vertical tip excursion as a function of the DC sample voltage for a fixed DC of 70 pA, inspired from measurements on bilayer NaCl on Ag(111). The inset shows the corresponding simulated $dI/dV(V)$ assuming a modulation voltage of 0.5 V. (b) Simulated THz current as a function of DC sample voltage for different amplitudes of the transient voltage V_{THz} (see the legend). (c) Maximum THz current obtained for different THz amplitudes V_{THz}. The inset shows the DC voltage at which the maximum THz current is reached for each V_{THz}. The horizontal dashed line indicates a THz current of 1 fA, providing an estimate of the experimental detection limit.

yielding

$$I_0 = f(V)\,\exp[-2\kappa\Delta z(V)], \quad (5)$$

and thus $f(V) = I_0 \exp[2\kappa\Delta z(V)]$.

This allows us to reconstruct an effective constant-height current–voltage characteristic at a reference height $\Delta z_0 = \Delta z(V_0)$,

$$\tilde{I}(V, \Delta z_0) = f(V)\exp(-2\kappa\Delta z_0) \tag{6}$$

$$= I_0 \exp[2\kappa(\Delta z(V) - \Delta z(V_0))]. \tag{7}$$

For $V = V_0$, one recovers $\tilde{I} = I_0$, as required. For clarity, we rewrite Eq. (7) as

$$\tilde{I}(V(t), \Delta z(V_{DC})) = I_0 \exp[2\kappa(\Delta z(V(t)) - \Delta z(V_{DC}))], \tag{8}$$

where V_{DC} sets the tip–sample distance via the feedback loop and $V(t)$ denotes the total voltage including the transient. In the limit $V(t) \to V_{DC}$, one obtains $\tilde{I} = I_0$, as expected. The transient current is then given by

$$i_{THz}(t) = \tilde{I}(V(t), \Delta z(V_{DC})) - I_0, \tag{9}$$

and the corresponding THz current is obtained from Eq. (3).

Figure 2(b) shows THz spectra computed for different transient amplitudes V_{THz}. A relatively low setpoint current of 70 pA is used and we used $\kappa = 0.37$ Å^{-1}, which is motivated by experimental measurements, discussed in Sec. III A. The spectra exhibit a broad peak between ≈3 and 4 V, corresponding to the voltage range where $\Delta z(V_{DC})$ varies most strongly. For $V_{THz} = 0.02$ V, the peak reaches ≈10 fA, while it exceeds 1 pA for $V_{THz} = 0.5$ V. With increasing V_{THz}, both the peak position shifts to higher V_{DC} and the peak width increases.

To quantify these trends, Fig. 2(c) shows the maximum THz current as a function of V_{THz}, with the corresponding V_{DC} values indicated in the inset. The maximum current is highly sensitive to V_{THz}. For instance, it increases by one order of magnitude, from 10 to 100 fA, when V_{THz} is increased from 0.02 to 0.12 V. A further increase to $V_{THz} = 0.37$ V raises the maximum THz current to ∼1 pA. These values remain relatively small due to the low setpoint current $I_0 = 70$ pA, but the relative signal is significant (e.g., $\sim 10^{-3}$ for $V_{THz} = 0.1$ V and ∼ 3% for $V_{THz} = 0.5$ V). Therefore, although the tip retracts during constant-current measurements, the ratio between the THz current and the setpoint current is enhanced (within a certain voltage range and for small THz amplitudes), thereby facilitating lock-in detection of the THz current.[34]

A key advantage of this approach is that several observables—the peak amplitude of $I_{THz}(V_{DC})$, its position, width, and onset—all depend on V_{THz}. This redundancy improves the robustness of the experimental determination of V_{THz}.

The behavior of $I_{THz}(V_{DC})$ can be understood qualitatively as follows. At low voltages, the nearly linear $I(V_{DC})$ characteristic does not rectify the transient voltage much, resulting in a very small THz current. Around $V_{DC} \approx 2.5$–2.7 V, the nonlinearity becomes accessible within the range V_{DC} to $V_{DC} + V_{THz}$, leading to an increasing THz current. At higher voltages ($V_{DC} \gtrsim 3.2$ V), the THz current decreases despite the persistence of nonlinearity. This results from the combined effects that (i) both I_{DC} and I_{THz} decay exponentially with increasing tip–sample distance, (ii) the variation of I_{DC} reflects the local electronic structure at V_{DC}, and (iii) I_{THz} depends on the nonlinearity of $I(V)$ over the interval $[V_{DC}, V_{DC} + V_{THz}]$. In this regime, the nonlinearity does not increase further (and may even decrease), while the tip retracts significantly, leading to an overall suppression of I_{THz}.

III. EXPERIMENTS

A. Characterization of the NaCl bilayer

NaCl deposited on Ag(111) grows in the form of bilayer islands.[35,36] NaCl is essentially insulating, with an electronic bandgap extending from ≈−5 to ≈3 V (Ref. 35). At intermediate voltages, however, the finite thickness of the NaCl bilayer still allows tunneling into the underlying Ag(111) substrate.

Figure 3(a) shows a representative STM image of the Ag(111) surface after NaCl deposition. Three roughly square bilayer islands with lateral dimensions of ≈50 nm are observed, with the upper-right island spanning a step edge of the Ag(111) surface. The corresponding height profile across the lower-right island is shown in Fig. 3(b), yielding an apparent height of 3.5 Å at 2 V.

Constant-height current–voltage characteristics measured on such islands exhibit an almost vanishing current up to sample voltages of ≈3.2 V, followed by a sharp increase in tunneling

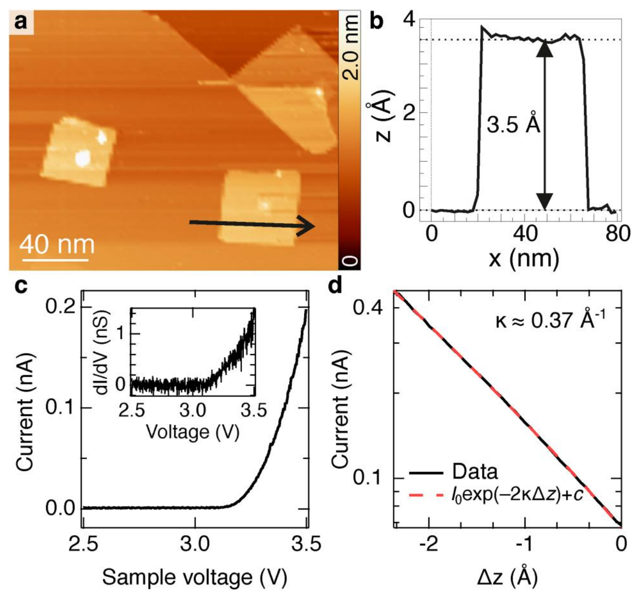

FIG. 3. Experimental characterization of the NaCl/Ag(111) sample. (a) Representative topograph of Ag(111) decorated with 2-ML-high NaCl bilayer islands, one of which spans a step edge. The image was acquired at 2 V and a constant current of 60 pA. (b) Height profile along the arrow indicated in (a). The NaCl island exhibits an apparent height of 3.5 Å. (c) Current–voltage characteristic measured on top of one island (constant-height measurement, feedback loop opened at 3.5 V and 0.2 nA). The inset shows the simultaneously acquired *dI/dV*, obtained using a root-mean-square modulation voltage of 0.5 V. (d) Current as a function of tip retraction Δz measured at 3 V. The feedback loop was opened at 3 V and 0.07 nA, defining the reference position for the tip–sample distance (Δz = 0).

current [Fig. 3(c)]. This transition to a nonlinear regime is exploited here to calibrate the amplitude V_{THz}. The simultaneously acquired dI/dV spectrum shows a corresponding onset, as expected. We note that the onset voltage varies slightly between islands, likely due to differences in lateral size and associated electronic properties.

The effective decay constant κ of the tunneling current is a key parameter for the proposed V_{THz} calibration. We, therefore, measured the current as a function of tip displacement Δz, as shown in Fig. 3(d) (black curve). The data are well described by $I_0 \exp(-2\kappa\Delta z) + c$ (red curve), confirming the exponential dependence of the tunneling current on the tip–sample distance assumed in the model above. The fit yields $\kappa = 0.37$ Å^{-1}, which is used in the following analysis. The measurement was performed at $V_{DC} = 3$ V, i.e., in the relevant voltage range. This ensures that any reduction of the effective barrier height at high voltage is effectively incorporated into the extracted value of κ, without requiring additional corrections.

Indeed, a value of κ close to 1 Å^{-1} is typically expected for a clean metal surface at low voltage.[33] Using $\kappa = \sqrt{2m\phi_a}/\hbar$, this corresponds to an apparent barrier height of $\phi_a \approx 3.85$ eV, which at low voltage is commonly interpreted as the average of the tip and sample work functions. At higher sample voltages, however, the apparent barrier height on coinage metal surfaces decreases significantly, reaching values of $\approx$1 eV near 4 V.[37] Furthermore, measurements on bilayer NaCl islands on Cu(311) report a reduction of the apparent barrier height by $\sim$30%, down to $\approx$2.8 eV compared to the bare metal surface. In the present case, the apparent barrier height is estimated to be on the order of 0.45 eV, reflecting the combined effect of the large sample voltage ($\approx$3 V) and the presence of the NaCl layer. It is worth noting that such a low apparent barrier height indicates that the junction operates close to the field-emission regime.

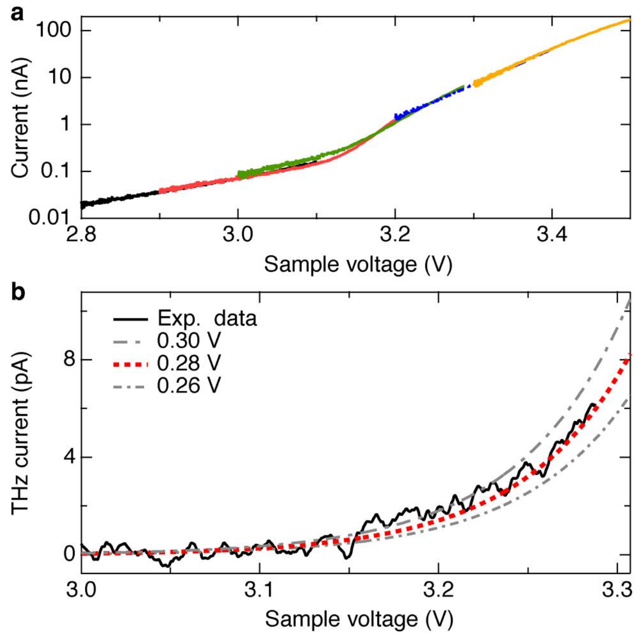

FIG. 4. Experimental DC and THz currents in constant-height measurements. (a) Reconstructed current–voltage characteristic measured on a NaCl island over an extended dynamic current range. The data combine several voltage sweeps (shown in different colors), each acquired over a limited voltage range at a fixed tip–sample distance. All sweeps are scaled relative to the first one, yielding the $I(V)$ characteristic corresponding to opening the feedback loop at $V = 2.8$ V and $I = 0.2$ nA. (b) Measured constant-height THz spectrum (black), compared with three simulations ($V_{THz} = 0.26$, 0.28, and 0.30 V).

B. Constant-height spectra

We first employ the standard $I(V)$ rectification approach to determine V_{THz}. At large sample voltages ($V_{DC} \approx 3.5$ V), the current typically has to remain below $\lesssim$0.2 nA to avoid damaging the NaCl islands. Under these conditions, the dynamic range of the transimpedance amplifiers typically used in STM experiments is insufficient to capture the full variation of the current–voltage characteristic, particularly near and below the onset of the nonlinearity. For example, in Fig. 3(c), the current for $V_{DC} \lesssim 3.2$ V is at the noise level of the amplifier, preventing a reliable measurement of its variation.

To overcome this limitation, we acquired the $I(V)$ characteristic in segments. Before each segment, the tip height was adjusted to keep the current within the measurable dynamic range. The full characteristic was then reconstructed by scaling the individual segments such that the overlapping voltage regions match. The result is shown in Fig. 4(a), where different colors indicate different segments. Between 2.8 and 3.5 V, the current spans approximately five orders of magnitude. A similar procedure has been employed previously.[28]

The reconstruction is not perfect. For instance, the red and green segments should overlap, but exhibit noticeable deviations, particularly in regions of strong nonlinearity. A single $I(V)$ characteristic is constructed by combining the individual segments and averaging them in the overlapping regions. The resulting characteristic is then slightly smoothed and, for practical reasons, extrapolated toward lower and higher voltages by extending the exponential behavior, which appears as a linear trend in the semi-logarithmic representation. The resulting $I(V)$ characteristic used for the simulations is shown in Fig. 7.

Figure 4(b) shows a representative constant-height THz spectrum. The signal is close to zero at low sample voltages and increases approximately exponentially, reaching 6 pA near 3.3 V. This behavior is consistent with expectations: a finite THz current appears once $V_{DC} + V_{THz}$ reaches the nonlinear regime of $I(V)$.

Constant-height THz spectra were simulated using Eqs. (2) and (3) for $V_{THz} = 0.26$, 0.28, and 0.30 V [dashed curves in Fig. 4(b)]. The best agreement with the experimental data is obtained for $V_{THz} = 0.28$ V (red curve), while $V_{THz} = 0.26$ and 0.30 V provide lower and upper bounds. Considering only the agreement between the simulations and the experimental data, the uncertainty appears relatively small, on the order of $\pm$0.02 V. However, additional sources of uncertainty must be considered, such as the accuracy of the reconstructed high-dynamic-range $I(V)$ characteristic [Fig. 4(a)], or whether the tip–sample distance used for the reconstructed $I(V)$ precisely matches that of the measured THz spectrum.

Quantifying these uncertainties is challenging because, in the present case, the analysis relies solely on the shape of $I_{\mathrm{THz}}(V_{\mathrm{DC}})$. For larger transient amplitudes V_{THz} and sharper nonlinearities, the onset of the THz spectrum would provide an additional independent observable. This is not the case here for smaller amplitudes. We, therefore, only provide an estimate of the transient voltage amplitude, on the order of 0.25 V, rather than a precise value.

C. Constant-current spectra

As described in Sec. II B, the electronic information in constant-current spectroscopy is encoded in the $\Delta z(V)$ dependence. Figure 5(a) shows a representative spectrum acquired on a bilayer NaCl/Ag(111) at a constant current $I_0 = 70$ pA. From $V_{\mathrm{DC}} = 2.6$ to ≈ 3.1 V, the tip retracts approximately linearly with increasing V_{DC}. Above this range, the retraction becomes more pronounced as tunneling into the conduction band of NaCl sets in, followed by a more gradual variation for $V_{\mathrm{DC}} > 3.2$ V.

The simultaneously measured THz current is shown in Fig. 5(b). I_{THz} is essentially zero at low voltages, starts to increase at $V_{\mathrm{DC}} \approx 2.9$ V, reaches a maximum slightly below 3.1 V, and decreases again to nearly zero for $V_{\mathrm{DC}} > 3.2$ V.

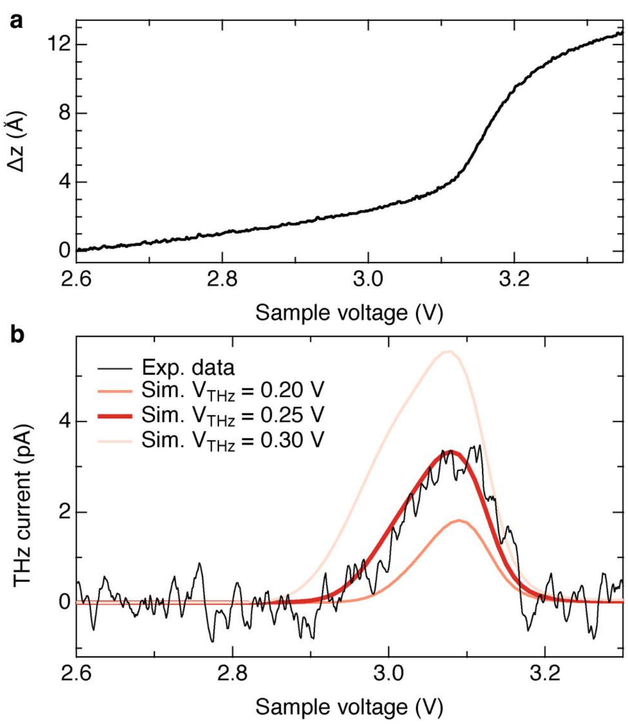

FIG. 5. Experimental constant-current THz spectrum. (a) Tip retraction as a function of sample voltage with the feedback loop active, regulating to a DC of 70 pA. (b) Simultaneously measured THz spectrum (black). The colored curves show simulations of THz spectra using the tip retraction shown in (a) and assuming three THz voltage amplitudes ($V_{\mathrm{THz}} = 0.20$, 0.25, and 0.30 V).

Using Eqs. (3) and (9), we simulate the THz spectra for $V_{\mathrm{THz}} = 0.20$, 0.25, and 0.30 V (red tones in Fig. 5). The simulation for $V_{\mathrm{THz}} = 0.25$ V (red curve) reproduces the experimental spectrum well, capturing both the peak amplitude and width, as well as the onset of the signal. In contrast, $V_{\mathrm{THz}} = 0.20$ V yields a peak that is too small and too narrow, with an onset at higher voltage. For $V_{\mathrm{THz}} = 0.30$ V, the simulated peak is too large and too broad, and the onset occurs at lower voltage. Based solely on the agreement between the simulations and the experimental data, the uncertainty in the THz amplitude is estimated to be on the order of 0.01 V.

These three simulations highlight that, in this measurement mode, V_{THz} is encoded not only in the amplitude of the THz spectrum, but also in the peak width and onset. In the following, we analyze how these observables, as well as the voltage at which the THz spectrum reaches its maximum, depend on the transient amplitude V_{THz}. Although the tunneling decay constant κ was inferred experimentally, we also consider its variability and show that an accurate calibration of V_{THz} does not require precise knowledge of κ.

Figures 6(a)–6(d) show the peak amplitude, peak width, peak position, and peak onset of the THz spectrum as functions of both V_{THz} and κ, displayed as two-dimensional maps where the color encodes the corresponding values. All maps are obtained from simulations based on the experimental constant-current $\Delta z(V)$ curve shown in Fig. 5(a). The peak onset provides the most intuitive observable, as it depends only weakly on κ. With increasing V_{THz}, the onset shifts to lower voltages, since the nonlinear regime is reached when $V_{\mathrm{DC}} + V_{\mathrm{THz}}$ exceeds the threshold. A similar trend is observed for the peak position, but with a significantly smaller variation. Over a V_{THz} range of 0.6 V, the peak position shifts by only ≈ 0.04 V, whereas the onset varies by ≈ 0.3 V. We, therefore, conclude that the peak position is of limited practical use for calibrating V_{THz}.

We next consider the experimentally determined values from the spectrum shown in Fig. 5(b): a THz current amplitude of 3.33 ± 0.5 pA, a full width at half maximum of 0.13 ± 0.1 V, and an onset voltage of 2.94 ± 0.1 V. We then identify the combinations of V_{THz} and κ that reproduce these observables. In Fig. 6(e), the green, red, and blue curves correspond to the parameter sets yielding the correct amplitude, peak width, and onset, respectively. The curves intersect at $\kappa \approx 0.38$ Å^{-1}, in excellent agreement with the independently measured value of 0.37 Å^{-1}, and at $V_{\mathrm{THz}} \approx 0.25$ V.

This value is slightly lower than the $V_{\mathrm{THz}} = 0.28$ V obtained from the constant-height method [Fig. 4(b)]. Since the THz excitation conditions were not intentionally modified, both measurements are expected to yield comparable amplitudes. The discrepancy may arise from differences in tip termination, which can affect the coupling of the THz field and thus the effective transient voltage. Alternatively, it may reflect limitations of the constant-height approach, where reconstructing $I(V)$ over a large dynamic range—particularly across sharp changes in conduction—introduces additional uncertainty.

Journal of Applied Physics ARTICLE pubs.aip.org/aip/jap

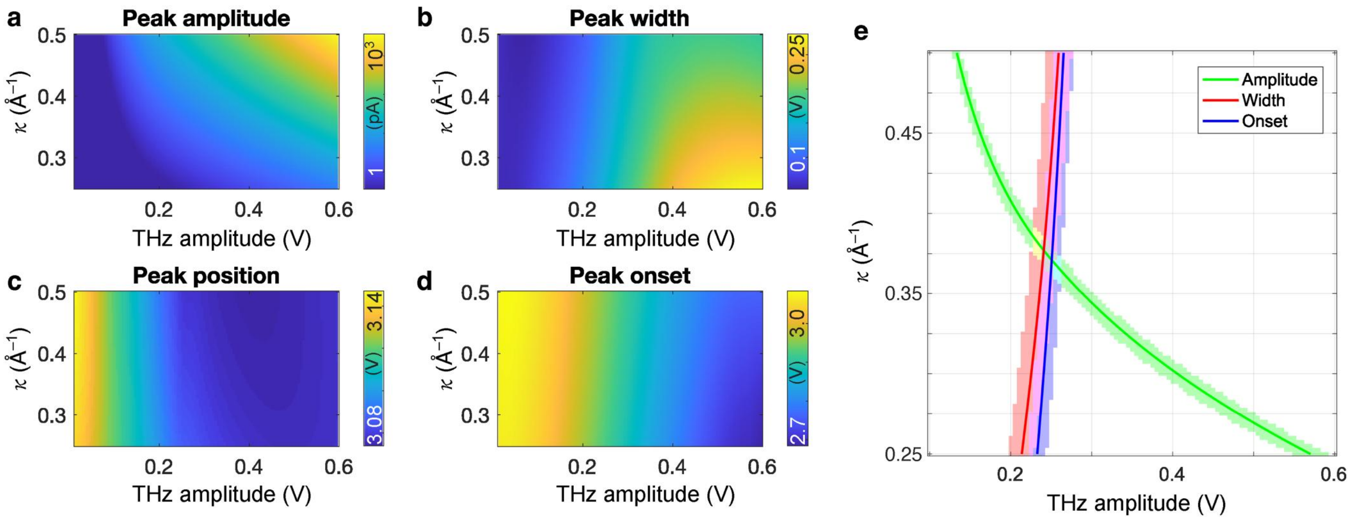

FIG. 6. Influence of the parameters in reproducing the THz current profile. Simulations such as those shown in Fig. 5(b) were performed for a wide range of tunneling decay constants κ and THz voltage amplitudes V_{THz}. From the simulated THz current profiles as a function of the DC sample voltage, the maps in (a)–(d) show, in a color-coded representation, the peak amplitude (pA), the full width at half maximum (V), the sample voltage at which the current reaches its maximum (V), and the onset voltage at which the peak reaches 10% of its maximum value. (e) Combinations of decay constant κ and THz amplitude V_{THz} reproducing the experimental peak amplitude of 3.33 ± 0.5 pA (green curve), the experimental full width at half maximum of 0.13 ± 0.1 V (red curve), and the onset voltage of 2.94 ± 0.1 V (blue curve). The colored regions indicate the uncertainty of the parameters obtained when propagating the experimental uncertainties of these quantities. The combined constraints significantly reduce the accessible parameter space and indicate that the value $\kappa = 0.37$ Å^{-1} used above is reasonable, while the corresponding THz voltage amplitude V_{THz} is on the order of 0.25 V.

We can nonetheless conclude that the THz setup used here provides a transient voltage amplitude on the order of $V_{THz} \approx 0.25$ V.

The methodology for calibrating the THz amplitude may be summarized as follows. $\Delta z(V_{DC})$ and THz spectra are acquired under a constant current I_0 in the voltage range of the nonlinearity. The decay constant κ can be independently determined from an $I(z)$ measurement performed at, or close to, the nonlinear region. If the near-field THz waveform is not known from auxiliary measurements, it may be approximated using Eq. (1). In the present case, the detailed shape of the waveform was found not to play a significant role in the determination of the THz amplitude (see Appendix D).

The THz spectra are then simulated using Eqs. (3), (7), and (9), and V_{THz} is adjusted until satisfactory agreement with the experimental spectra is obtained. Among the different observables, the onset, peak width, and peak amplitude are particularly relevant. The onset is likely the least sensitive to uncertainties in the exact THz waveform.

IV. CONCLUSION

Using a combination of simulations and experimental data, we have analyzed different methods to calibrate the amplitude of THz-induced voltage transients, with particular emphasis on small amplitudes. These approaches rely on the nonlinearity of the current–voltage characteristic, which is required for rectification and, thus, for the detection of a THz current. In the standard approach, I_{THz} is measured as a function of V_{DC} at *constant tip–sample distance*. In this configuration, the onset of the $I(V)$ characteristic is shifted by V_{THz}, or the THz spectra are reconstructed from $I(V)$ assuming a given transient waveform. However, both strategies exhibit significant limitations for small V_{THz}. The onset is often poorly defined due to the intrinsic broadening of spectroscopic features, and reconstruction methods require accurate knowledge of $I(V)$ over a wide dynamic range, where small inaccuracies can lead to large uncertainties in V_{THz}.

We instead propose a method based on constant-current measurements, together with a corresponding reconstruction scheme. As demonstrated experimentally for a NaCl bilayer on Ag(111) at the onset of the conduction band, the resulting THz spectra exhibit a broad peak. The peak amplitude, width, and onset are all directly related to V_{THz}, providing multiple observables for its determination and thereby improving robustness, particularly at small amplitudes. In addition, this approach enables the use of nonlinearities in $I(V)$ occurring at large DC voltages. Constant-current operation allows measurements over a wide dynamic range while maintaining low DCs, thereby avoiding instability or damage of the STM junction that would otherwise occur in constant-height measurements at high voltages. Overall, this method provides a reliable framework for calibrating THz-induced voltage transients, especially in the regime of small amplitudes.

V. METHODS

The THz-STM setup employed in this work is described in Ref. 10. THz radiation is generated using a femtosecond fiber laser (T-Light, Menlo Systems) combined with photoconductive antennas based on InGaAs/InAlAs heterostructures. The system employs a pair of photoconductive antennas, typically used for pump–probe operation, whose outputs are focused onto the STM junction. In the present experiments, the relative delay between the pulses was adjusted to maximize the transient field amplitude. The repetition rate of the system is $f_{\text{Rep}} = 100\,\text{MHz}$. For a THz current of ≈3 pA, this corresponds to a net transfer of only ≈0.2 electrons per pulse. The lifetime of electrons in the NaCl conduction band is expected to be ultrashort, and in any case much shorter than both the interval between successive THz pulses (10 ns) and the average time between tunneling electrons associated with the DC (≈3 ns for 70 pA). We, therefore, assume that the system relaxes back to equilibrium between successive THz excitations.

The home-built STM was operated in ultrahigh vacuum at a temperature of ≈8 K. The STM tips were fabricated from W wire and conditioned by indentation into the Ag(111) surface.

The Ag(111) substrate was cleaned *in situ* by repeated cycles of Ne^+ sputtering and annealing to 530 °C. NaCl was subsequently deposited from a Knudsen cell held at 565 °C, while the sample was maintained at room temperature.

ACKNOWLEDGMENTS

This work was funded by the Deutsche Forschungsgemeinschaft (DFG, German Research Foundation) through Project No. 278162697 (SFB 1242).

AUTHOR DECLARATIONS

Conflict of Interest

The authors have no conflicts to disclose.

Author Contributions

Hüseyin Azazoglu: Data curation (equal); Investigation (lead); Visualization (equal); Writing – review & editing (equal). **Rolf Möller:** Data curation (equal); Investigation (equal); Methodology (equal); Validation (equal); Writing – review & editing (equal). **Manuel Gruber:** Conceptualization (equal); Data curation (equal); Formal analysis (equal); Funding acquisition (equal); Investigation (equal); Methodology (equal); Project administration (equal); Software (equal); Supervision (equal); Validation (equal); Visualization (equal); Writing – original draft (equal).

DATA AVAILABILITY

The data that support the findings of this study are available from the corresponding author upon reasonable request.

APPENDIX A: CONSTANT-HEIGHT *I–V* CURVES

We consider two phenomenological models $I(V)$ describing a transition from a linear low-voltage regime to an exponential increase above a threshold voltage V_t. This mimics, to some extent, experimental spectra on NaCl/Ag(111), where the exponential onset corresponds to tunneling into the conduction band of NaCl, while the linear behavior below V_t accounts for finite tunneling within the bandgap.

The linear regime does not rectify THz-induced transient voltages and, therefore, does not generate a THz current. A THz current is only observed when the transient voltage reaches the nonlinear regime. This property has been used to calibrate large transient voltages. Its applicability at low amplitudes depends on the sharpness of the transition between the linear and exponential regimes. The two models introduced below describe different transition smoothness.

The simplest model is a piecewise linear–exponential function,

$$I_1(V) = \begin{cases} A\,m\,V, & V \le V_t, \\ A\,m\,V_t\,\exp(k(V - V_t)), & V > V_t, \end{cases} \tag{A1}$$

which is continuous at V_t but exhibits a discontinuity in its first derivative.

To obtain a smooth transition, we introduce a regularized positive-part function

$$g_\sigma(V) = \frac{1}{2}\left[(V - V_t) + \sqrt{(V - V_t)^2 + \sigma^2}\right], \tag{A2}$$

which interpolates smoothly between 0 for $V \ll V_t$ and $V - V_t$ for $V \gg V_t$. The corresponding smooth current is defined as

$$I_2(V) = A\,m\,V + A\,m\,V_t\left[\exp(k\,g_\sigma(V)) - \exp(k\,g_\sigma(0))\right]. \tag{A3}$$

This construction ensures $I_2(0) = 0$, reproduces the linear behavior $I_2(V) \approx A\,m\,V$ for $V \ll V_t$, and recovers the same asymptotic exponential behavior as I_1 for $V \gg V_t$. A third model, I_3, is obtained by increasing the smoothing parameter from $\sigma = 0.1$ V to $\sigma = 0.3$ V, leading to a broader and more gradual transition region while preserving the same low- and high-voltage asymptotics. For the curves shown in Fig. 1(a), we use $V_t = 3.0$ V, $m = 0.0004$, $k = 6\,\text{V}^{-1}$, and $A = 1250$ nA/V.

APPENDIX B: CONSTANT-CURRENT *Z–V* CURVES

We assume an exponential dependence of the tunneling current on the tip–sample distance,

$$I = I_0 \exp(-2\kappa\Delta z), \tag{B1}$$

which can be inverted as

$$\Delta z = -\frac{1}{2\kappa}\ln\left(\frac{I}{I_0}\right). \tag{B2}$$

We model the density of states by a Gaussian centered at $V_0 = 3.67$ V with a standard deviation $\sigma_0 = 0.26$ V and consider

$$\Delta z(V) = -\frac{1}{2\kappa}\ln\left(\int_0^{V_{\text{DC}}} dV\,\exp\left[-\left(\frac{V - V_0}{\sqrt{2}\sigma_0}\right)^2\right] + m\right) + z_0.$$

This expression mimics the experimentally observed $\Delta z(V)$ for a NaCl bilayer on Ag(111). The parameter $m = 0.0004$ introduces a finite tunneling contribution within the NaCl bandgap. The offset z_0 is chosen such that $\Delta z = 0$ at $V = 1$ V. We use $\kappa = 0.37$ Å^{-1}, as inferred experimentally [see Fig. 3(d)]. The resulting $\Delta z(V)$ curve is shown in Fig. 2(a).

APPENDIX C: EXTENDED RANGE FOR *I*–*V*

Figure 7 shows the extended *I*–*V* characteristic used to compute the constant-height spectra in Fig. 4(b). The characteristic is extrapolated toward lower and higher sample voltages, which is required to evaluate the THz signal over the full voltage range of interest. For example, determining I_{THz} at $V_{\mathrm{DC}} = 3.5$ V requires knowledge of $I(V)$ up to $V_{\mathrm{DC}} + V_{\mathrm{THz}}$.

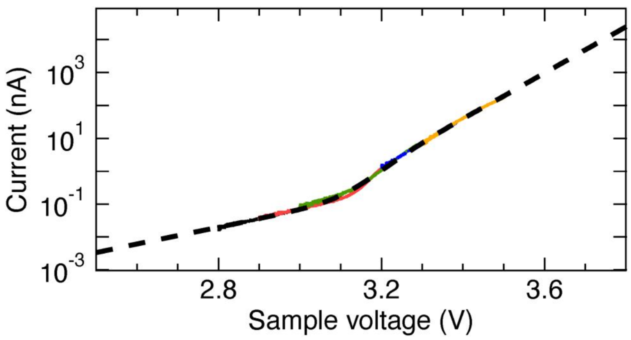

FIG. 7. Extended *I*–*V* characteristic. The colored lines represent individual constant-height sweeps acquired over limited voltage ranges. The scaling procedure follows Fig. 4(a). The dashed line shows the composite *I*–*V* characteristic used for the simulations at constant height. For voltages below 2.8 V and above 3.5 V, the curve was extended by linear fits to the logarithmic data.

APPENDIX D: DEPENDENCE OF V_{THz} DETERMINATION ON THE TRANSIENT WAVEFORM

The simulations of the THz spectra presented in the paper were performed using a specific transient-voltage waveform [shown in Fig. 1 and reproduced in Fig. 8(a) as the black curve], computed using Eq. (1) with $A_2 = 1/1.4$. This waveform corresponds to a predominantly unipolar pulse and mimics the THz waveform measured experimentally in the far field.[10]

In this section, we additionally consider a more bipolar-like pulse [red curve in Fig. 8(a)], generated with the same positive peak amplitude as the previous waveform (0.25 V in the present case). The corresponding THz spectrum, shown in Fig. 8(b), differs only weakly from the unipolar case. The amplitude increases by approximately 7%, while the overall spectral shape remains very similar. In particular, no significant shift of the onset or peak position is observed.

This weak dependence of the THz spectrum on the waveform can be understood as follows. The shape and amplitude of the THz spectrum are primarily governed by the largest positive excursions of the transient voltage. When the negative part of the waveform would contribute significantly to the rectification process, the tip has already retracted to maintain the DC constant.

The moderate increase in THz-current amplitude obtained with the bipolar waveform originates from the effectively broader positive portion of the pulse, which generates additional rectified current. The amplitude of the THz spectrum could, therefore, potentially provide information about the temporal width of the relevant positive part of the transient voltage.

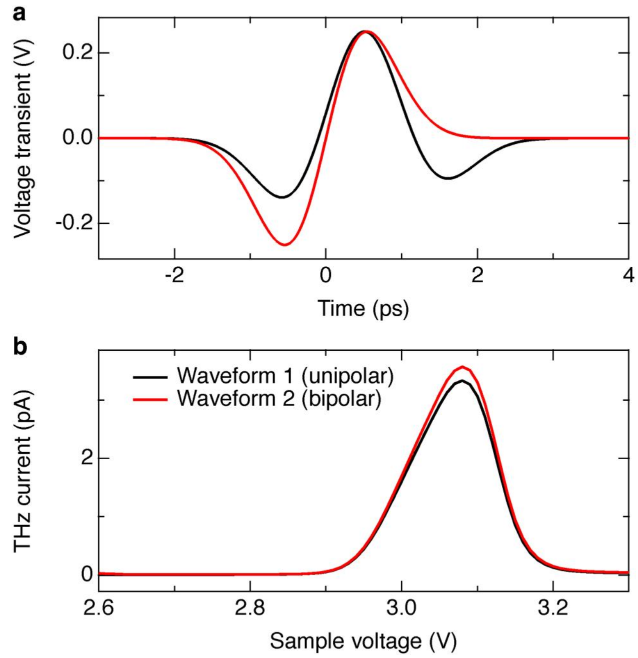

FIG. 8. Unipolar vs bipolar waveforms. (a) Voltage-transient waveforms corresponding to a unipolar (black) and bipolar (red) pulse, generated using Eq. (1) with $A_2 = 1/1.14$ and $A_2 = 0$, respectively. The amplitudes are scaled to reach 0.25 V. (b) Simulated THz spectra obtained using the waveforms shown in (a) together with the $\Delta z(V_{\mathrm{DC}})$ spectrum from Fig. 4(a).

REFERENCES

[1]T. L. Cocker, V. Jelic, M. Gupta, S. J. Molesky, J. A. J. Burgess, G. D. L. Reyes, L. V. Titova, Y. Y. Tsui, M. R. Freeman, and F. A. Hegmann, Nat. Photonics **7**, 620 (2013).
[2]S. Grafström, J. Kowalski, R. Neumann, O. Probst, and M. Wörtge, J. Vac. Sci. Technol. B **9**, 568 (1991).
[3]S. Grafström, P. Schuller, J. Kowalski, and R. Neumann, J. Appl. Phys. **83**, 3453 (1998).
[4]S. Grafström, J. Appl. Phys. **91**, 1717 (2002).
[5]H. Azazoglu, R. Möller, and M. Gruber, Surf. Sci. **743**, 122465 (2024).
[6]S. Yoshida, H. Hirori, T. Tachizaki, K. Yoshioka, Y. Arashida, Z.-H. Wang, Y. Sanari, O. Takeuchi, Y. Kanemitsu, and H. Shigekawa, ACS Photonics **6**, 1356 (2019).
[7]M. Müller, N. M. Sabanés, T. Kampfrath, and M. Wolf, ACS Photonics **7**, 2046 (2020).
[8]S. Banerjee and P. Zhang, Phys. Rev. Appl. **18**, 024011 (2022).

[9]Y. Luo, V. Jelic, G. Chen, P. H. Nguyen, Y.-J. R. Liu, J. A. M. Calzada, D. J. Mildenberger, and F. A. Hegmann, Phys. Rev. B **102**, 205417 (2020).
[10]H. Azazoglu, P. Kapitza, M. Mittendorff, R. Möller, and M. Gruber, Rev. Sci. Instrum. **95**, 023703 (2024).
[11]T. L. Cocker, D. Peller, P. Yu, J. Repp, and R. Huber, Nature **539**, 263 (2016).
[12]S. Sheng, M. Abdo, S. Rolf-Pissarczyk, K. Lichtenberg, S. Baumann, J. A. J. Burgess, L. Malavolti, and S. Loth, Nat. Phys. **20**, 1603 (2024).
[13]V. Jelic, S. Adams, D. Maldonado-Lopez, I. A. Buliyaminu, M. Hassan, J. L. Mendoza-Cortes, and T. L. Cocker, Nat. Photonics **19**, 1048 (2025).
[14]C. Roelcke, L. Z. Kastner, M. Graml, A. Biereder, J. Wilhelm, J. Repp, R. Huber, and Y. A. Gerasimenko, Nat. Photonics **18**, 595 (2024).
[15]V. N. Rai, J. Sim, F. Faaber, N. Bogdanoff, S. Trishin, P. Wiechers, T. S. Seifert, T. Kampfrath, C. Lotze, and K. J. Franke, Sci. Adv. **11**, eadz6549 (2025).
[16]L. Wang, Y. Xia, and W. Ho, Science **376**, 401 (2022).
[17]D. Peller, L. Z. Kastner, T. Buchner, C. Roelcke, F. Albrecht, N. Moll, R. Huber, and J. Repp, Nature **585**, 58 (2020).
[18]S. Sheng, A.-C. Oeter, M. Abdo, K. Lichtenberg, M. Hentschel, and S. Loth, Phys. Rev. Lett. **129**, 043001 (2022).
[19]S. E. Ammerman, V. Jelic, Y. Wei, V. N. Breslin, M. Hassan, N. Everett, S. Lee, Q. Sun, C. A. Pignedoli, P. Ruffieux, R. Fasel, and T. L. Cocker, Nat. Commun. **12**, 6794 (2021).
[20]R. Gutzler, M. Garg, C. R. Ast, K. Kuhnke, and K. Kern, Nat. Rev. Phys. **3**, 441 (2021).
[21]T. L. Cocker, V. Jelic, R. Hillenbrand, and F. A. Hegmann, Nat. Photonics **15**, 558 (2021).
[22]M. Müller, Prog. Surf. Sci. **99**, 100727 (2024).
[23]S. Chen, W. Shi, and W. Ho, Nano Lett. **23**, 2915 (2023).
[24]S. Sheng, L. Chen, J. Schust, K. Lichtenberg, M. Abdo, F. Huber, S. Baumann, and S. Loth, Nano Lett. **24**, 15291 (2024).
[25]D. Peller, C. Roelcke, L. Z. Kastner, T. Buchner, A. Neef, J. Hayes, F. Bonafé, D. Sidler, M. Ruggenthaler, A. Rubio, R. Huber, and J. Repp, Nat. Photonics **15**, 143 (2021).
[26]H. Li, T. Wang, W. Wei, K. Zhang, J.-Y. Xu, Y. Wu, and G. Fang, ACS Photonics **11**, 1428 (2024).
[27]V. Jelic, S. Adams, M. Hassan, K. Cleland-Host, S. E. Ammerman, and T. L. Cocker, Nat. Photonics **18**, 898 (2024).
[28]V. Jelic, K. Iwaszczuk, P. H. Nguyen, C. Rathje, G. J. Hornig, H. M. Sharum, J. R. Hoffman, M. R. Freeman, and F. A. Hegmann, Nat. Phys. **13**, 591 (2017).
[29]L. Bobzien, J. Allerbeck, S. E. Ammerman, R. Torsi, J. A. Robinson, and B. Schuler, APL Mater. **12**, 051110 (2024).
[30]S. E. Ammerman, Y. Wei, N. Everett, V. Jelic, and T. L. Cocker, Phys. Rev. B **105**, 115427 (2022).
[31]M. Ziegler, N. Néel, A. Sperl, J. Kröger, and R. Berndt, Phys. Rev. B **80**, 125402 (2009).
[32]H. Pfeifer, B. Koslowski, and P. Ziemann, Beilstein J. Nanotechnol. **2**, 607 (2011).
[33]C. J. Chen, *Introduction to Scanning Tunneling Microscopy*, 2nd ed. (Oxford University Press, 2008).
[34]For measurements performed directly on Ag(111), we could not detect a sizable THz current near the surface-state onset (≈−60 meV), although rectification of the voltage transient is expected to occur. This is most likely because the ratio between the THz current and the comparatively large DC on metallic surfaces remains too small for reliable lock-in detection.
[35]S. Heidorn, C. Bertram, J. Koch, K. Boom, F. Matthaei, A. Safiei, J. Henzl, and K. Morgenstern, J. Phys. Chem. C **117**, 16095 (2013).
[36]K. Kolpatzeck, L. Brendel, R. Möller, R. Robles, and N. Lorente, Phys. Rev. B **107**, 155418 (2023).
[37]M. Becker and R. Berndt, Phys. Rev. B **81**, 035426 (2010).